MATERIALS SCIENCE

Large stroke radially oriented MXene composite fiber tensile artificial muscles

Junsong Fu[1,2,3]†, Yuchen Li[1,2,3]†, Tianzhu Zhou[4]†, Shaoli Fang[5]†, Mengmeng Zhang[5]†, Yanlei Wang[6]†, Kun Li[7], Wangwei Lian[1,2,3], Lei Wei[4], Ray H. Baughman[5]*, Qunfeng Cheng[1,2,3,8]*

Actuation is normally dramatically enhanced by introducing so much yarn fiber twist that the fiber becomes fully coiled. In contrast, we found that usefully high muscle strokes and contractile work capacities can be obtained for non-twisted MXene ($Ti_3C_2T_x$) fibers comprising MXene nanosheets that are stacked in the fiber direction. The MXene fiber artificial muscles are called MFAMs. We obtained MFAMs that have high modulus in both the radial and axial directions by spinning a solution containing MXene nanosheets dispersed in an aqueous cellulose solution. We observed a highly reversible muscle contraction of 21.0% for a temperature increase from 25° to 125°C. The tensile actuation of MFAMs mainly results from reversible hydrogen bond orientation change during heating, which decreases intra-sheet spacing. The MFAMs exhibited fast, stable actuation to multiple temperature-generating stimuli, which increases their applications in smart textiles, robotic arms, and robotic grippers.

INTRODUCTION

It is well known that twisted polymer fibers can serve as artificial muscles that provide giant torsional actuation (*1*–*3*). However, tensile actuation is very low until so much twist is inserted that the polymer fibers become coiled (*4*, *5*). If a large tensile stroke is needed for a modest temperature change, the only previous choice is to use a high-spring-index coiled polymer fiber or yarn. However, there are important problems associated with the use of high-spring-index coiled fibers. First, the only published way to obtain the needed high-spring-index coiled muscles is to wrap a twisted polymer fiber around a mandrel that has a much larger diameter than the polymer fiber (*6*–*10*). The problem is that there are no process reports for making mandrel-free large-spring-index yarns other than to dissolve the mandrel after muscle coiling, which wastes the large-diameter polymer fiber that is typically used as a mandrel and creates a waste stream (*11*, *12*). Second, the weight-normalized performance of these high-spring-index muscles, such as mechanical energy generation during a muscle stroke, is much lower than the weight-normalized energy generation of lower spring-index muscles (*13*, *14*). Third, many key applications of coiled artificial muscles involve their being woven into a base textile that contains polymer yarns having a diameter that is smaller than the separation between coils in the high-spring-index fibers, so slipping of the base textile yarns or fibers between the muscle coils can interfere with muscle actuation (*15*).

Transition metal carbides, specifically MXene ($Ti_3C_2T_x$), are a typical class of two-dimensional nanosheets fabricated by selectively etching and delaminating the MAX (Ti_3AlC_2) phase (*16*, *17*). These nanosheets have exceptional properties, including high electrical conductivity exceeding 10^5 S cm^{-1} and an impressive Young's modulus of 0.3 TPa (*18*–*20*). The surface of MXene nanosheets is rich in polar functional groups (-OH, -F, -O, etc.), which imparts hydrophilicity and enables the formation of extensive hydrogen bond networks with hydroxyl-containing polymers (*21*, *22*). Furthermore, their nearly 100% photothermal conversion efficiency and rapid Joule heating capabilities allow MXene nanosheets to be applied in various fields, such as sensors, electronic devices, and energy storage (*23*). Cellulose nanofibers (CNFs), which are renewable plant fibers characterized by high mechanical strength and a large surface area, also contain abundant hydroxyl functional groups (*24*, *25*). However, although the composite assembly of MXene nanosheets and CNFs into films has demonstrated some basic and weak transverse driving behaviors, achieving larger thermal actuation deformation in volume or length remains challenging. This limitation arises primarily from the driving behavior being based on differences in thermal expansion due to the asymmetric bilayer structure (*26*).

We here describe a previously undiscovered tensile fiber muscle type that provides large tensile actuation without needing twist insertion. While previous artificial muscle fibers have high elastic modulus only in the fiber direction, our recently found artificial muscles have a high modulus in both the fiber direction and the fiber radial direction. This high modulus in the fiber radial direction is realized by using a spinning process that is different from ordinary spinning processes, which orientate all high modulus components in the fiber direction. In the present fiber spinning process, we eliminate shear-induced stack-nanosheets orientation parallel to the spinning direction by using the device described by Lian's team (*27*). This device initially provides stack-nanosheets plane orientation parallel to the spinning direction and then expands the diameter of the spinning solution to provide stack-nanosheets orientation perpendicular to the spinning orientation before fiber solidification.

We here experimentally and theoretically describe how highly reversible large tensile actuation strokes and high contractile work capacities can be obtained for fibers having MXene nanosheets

[1]School of Chemistry, Key Laboratory of Bio-inspired Smart Interfacial Science and Technology of Ministry of Education, Beihang University, Beijing 100191, China. [2]School of Chemistry and Materials Science, University of Science and Technology of China, Hefei 230026, China. [3]Suzhou Institute for Advanced Research, University of Science and Technology of China, Suzhou 215123, China. [4]School of Electrical and Electronic Engineering, Nanyang Technological University, Singapore 639798, Singapore. [5]Alan G. MacDiarmid NanoTech Institute, University of Texas at Dallas, Richardson, TX 75080, USA. [6]School of Chemistry and Life Resources, Renmin University of China, Beijing 100872, China. [7]Beijing Key Laboratory of Ionic Liquids Clean Process, Institute of Process Engineering, Chinese Academy of Sciences, Beijing 100190, China. [8]Institute of Energy Materials Science (IEMS), University of Shanghai for Science and Technology, Shanghai 200093, China.
*Corresponding author. Email: ray.baughman@utdallas.edu (R.H.B.); cheng@buaa.edu.cn, chengqf@ustc.edu.cn (Q.F.C.)
†These authors contributed equally to this work.

oriented normal to the MXene fiber direction without inserting any fiber twist. These results also explain why tensile thermal actuation is dramatically enhanced without the need to insert such high twist that the fiber coils. The MXene fiber artificial muscles are called MFAMs. While previous high performance homochiral artificial muscles contract because of yarn volume expansion, which transfers yarn twist to coiling twist, such twist transfer is not possible for the present muscles since these new muscles are neither twisted nor coiled. In situ temperature–dependent characterization reveals that tensile contractions up to 21.0% are obtained for the MFAMs largely because of orientational rearrangement of the angles of the hydrogen bonds that connect neighboring MXene nanosheets. Since the MFAMs show high actuation when driven thermally by electrical or environmental heating or infrared light, they enable diverse actuation means for smart textiles and robotics.

RESULTS

Fabrication and characterization of the MFAMs

MXene nanosheets were synthesized by selectively etching the Al layer from MAX (Ti_3AlC_2) phase (fig. S1) (*28*). X-ray diffraction (XRD) patterns verified that the Al element was completely removed, as shown in fig. S2. According to the scanning electron microscope (SEM) and atomic force microscope (AFM) images in figs. S3 and S4, we obtained different lateral sizes exfoliated MXene nanosheets, while their thickness of ~1.6 nm is higher than that of normal nanosheets due to the -OH terminal groups and water molecules on the surface of exfoliated MXene nanosheets (*29*). Energy-dispersive x-ray spectroscopy mapping demonstrates the uniform distribution of Ti, O, C, and F elements and verifies the presence of -OH terminal groups and H_2O (fig. S5). High-resolution transmission electron microscope (HR-TEM) images and selected-area electron diffraction patterns demonstrate the expected highly crystalline hexagonal symmetry of the in-plane (100) MXene structure (fig. S6) (*30*). CNFs having a length of ~0.9 μm and a diameter of ~4.7 nm, which were prepared by ultrasonic dispersion, were used as cross-linkers to bridge MXene nanosheets (fig. S7). Surface microtopography shows that the CNFs are well distributed on the surface of MXene nanosheets (fig. S8), indicating the favorable dispersibility of the hybrid MXene/CNFs nanosheets in the solution. XRD shows an increased *d*-spacing (from 12.8 to 13.4 Å) for the hybrid MXene/CNFs nanosheets with the equal weight percentage ratio of 50:50 after the introduction of CNFs, compared with that of pure MXene nanosheets (fig. S9A). Moreover, Fourier-transform infrared (FTIR) spectroscopy spectra indicates that the wave number for the -OH vibrations of MXene nanosheets was shifted from ~3443.4 to ~3435.1 cm^{-1} in going from pure MXene to hybrid MXene/CNFs nanosheets, indicating the formation of hydrogen bonds between MXene and CNFs (fig. S9B) (*31*, *32*). In addition, x-ray photoelectron spectroscopy shows that the hybrid MXene/CNFs nanosheets had an ~6.48% increase in atomic percent of O compared to that in pure MXene nanosheets, supporting the presence of hydrogen bonds between these nanosheets (fig. S10 and table S1). Thermogravimetric analysis showed that the first weight loss (~1.6%) corresponds to the removal of water molecules from MXene nanosheets (fig. S11), confirming the existence of water molecules on the surface of MXene nanosheets. When the CNFs were introduced into MXene nanosheets to form the hybrid MXene/CNFs nanosheets, negligible weight loss of water up to 125°C was obtained compared to that of MXene nanosheets due to the hydrogen bond networks between MXene, H_2O, and CNFs (*33*).

Figure 1A illustrates the fabrication of the MFAMs having MXene nanosheets oriented approximately normal to the fiber direction. As shown in fig. S12, the MXene/CNFs ink exhibits typical shear thinning behavior, with MXene nanosheets self-assembling into randomly arranged liquid crystal domains (*34*, *35*). The liquid crystal phase of the MXene/CNFs ink is initially squeezed into a narrow channel, where the shear flow induces a horizontally oriented arrangement of the hybrid MXene/CNFs nanosheets, so the MXene nanosheets plane is approximately parallel to the fiber direction. Subsequently, when the ink is continuously pumped from the narrow channel to the expanded channel, the notable extensional stresses from the expansion flow enable the MXene nanosheets to arrange perpendicular to the flow direction (*28*, *36*). Last, the MFAMs featuring a radially oriented hierarchical structure (i.e., with MXene nanosheets approximately orthogonal to the fiber direction) was successfully obtained after undergoing the ethanol coagulation bath process. MFAMs had scalable fabricability since hundred meter–long fiber was easily produced (Fig. 1B). As shown in fig. S13, the MFAMs had a radial Herman's orientation factor (*f*) of 0.63 at 25°C, which was calculated from the wide-angle x-ray scattering (WAXS) patterns. The radially oriented hierarchical structure was additionally confirmed by surface and cross-sectional SEM images (Fig. 1C and fig. S14). To further investigate the internal structure of the MFAMs, we examined the morphology of a longitudinal section of the MFAMs fiber that was prepared for TEM measurement by focused ion beam milling, as shown in figs. S15 and S16. As shown in Fig. 1D, there are few voids distributed among the vertically aligned MXene nanosheets, as well as CNFs in the cross-linking layer between MXene nanosheets. Moreover, fig. S17 shows that the interlamellar spacing of out-of-plane (002) crystals for MXene nanosheets is about 1.452 nm (*37*) and the interplanar spacing of in-plane (110) crystals for CNFs is about 0.329 nm (*38*, *39*), further indicating that some CNFs are intercalated between MXene nanosheets to form hydrogen bond networks. Therefore, thanks to the hydrogen bond networks and the existing voids among the hybrid MXene/CNFs nanosheets with the radially oriented structure, the MFAMs undergo large contraction when heated, as shown in Fig. 1E and movie S1. When heated to 125°C, a single strand of the MFAM with the optimal ratio of MXene to CNFs (50:50 in wt %) (MFAM-II) can lift an object weighing about 1000 times its own weight, achieving a maximum tensile stroke of 21.0%, as well as the highest tensile strength (figs. S18 to S21 and table S2). Meanwhile, when subjected to a stress of ~13.0 MPa, the MFAMs demonstrated a high work capacity of ~1.76 J g^{-1}, which is about 45 times greater than that of mammalian skeletal muscles (~0.039 J g^{-1}), as shown in Fig. 1F. In addition, we prepared three kinds of MFAMs with MXene nanosheets of small (1.2 μm), medium (5.8 μm), and large (15.5 μm) sizes. When the tensile load was 0.64 MPa, the MFAMs show that the tensile stroke was ~17, ~21, and ~20%, while the work capacity was ~0.8, ~1.1, and ~ 1.1 J g^{-1}, respectively (fig. S22). These results indicate that the lateral size of MXene nanosheets does not significantly affect the actuation performance of MFAMs. The slightly lower actuation performance of the MFAMs with small size of MXene nanosheet might result from the fewer connection sites between the small size MXene nanosheets and the CNFs, which could provide a smaller stroke since these interconnections are needed for the "zipping" effect (*40*).

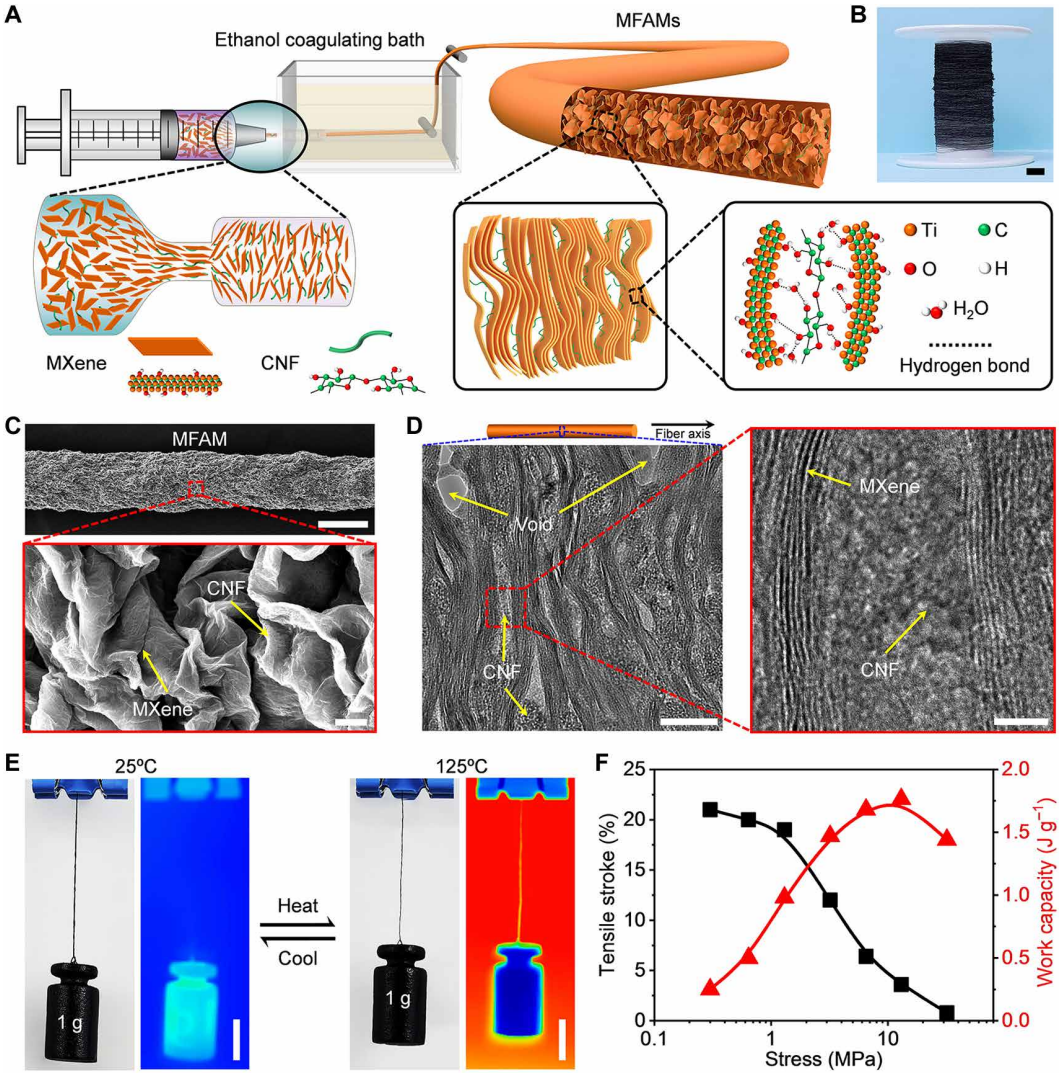

Fig. 1. Fabrication and characterization of the MFAMs. (**A**) Schematic illustration of the fabrication of the MFAMs. Under the notable extensional stresses, the hybrid MXene/CNFs nanosheets were aligned perpendicular to the MFAM fiber. (**B**) Photograph of a hundred-meter-long MFAM wound around a reel. (**C**) SEM images of the surface of an MFAM. (**D**) HR-TEM images of the longitudinal section for an MFAM. (**E**) Digital photographs and infrared thermal images of the reversible contractile actuation of an MFAM under heating and cooling. (**F**) Tensile stroke and work capacity versus the applied tensile stress on an MFAM. Scale bars, 1 cm (B), 100 μm (top) and 1 μm (bottom) (C), 50 nm (left), and 10 nm (right) (D), and 5 mm (E).

Contractile actuation mechanism of the MFAMs

The contractile actuation of the MFAMs was systematically studied through in situ temperature–dependent characterizations and molecular dynamics (MD) simulations. As shown in Fig. 2A and fig. S23, in situ WAXS patterns show that the radial orientation for MFAMs gradually increases from 0.63 to 0.73 upon heating from 25° to 125°C, indicating that the MXene nanosheets were flattening, thereby producing contractile actuation of the MFAMs. Note that the MFAMs exhibit a negative Poisson's ratio (−0.2) in the fiber direction, as well as a negative thermal expansion, when heated from 25° to 125°C. Simultaneously, according to in situ x-ray patterns, the *d*-spacing of the MFAMs decrease by about 1.7 Å during heating from 25° to 125°C (Fig. 2B, fig. S24, and table S3). Meanwhile, the porosity of MFAMs decreased from 37.3 to 30.5%, and the density increased from 1.22 to 1.51 g cm^{-3} (Fig. 2B and table S4). In situ AFM images revealed that the thickness of MXene nanosheets decreased by about 0.3 nm and the surface texture of the MXene nanosheets became smoother (fig. S25). These above results indicate that rearrangement of hydrogen bond networks occurs among MXene nanosheets, H_2O, and CNFs, which induces contractile actuation during heating. Furthermore, in situ temperature–dependent FTIR images show that the intensity of the -OH stretching vibration peak for MXene at ~3435.1 cm^{-1}, the -OH bending at ~1639.5 cm^{-1} for MXene/CNFs, and the H_2O at ~3244.2 cm^{-1} gradually decreased without shifting frequency as temperature increased from 25° to 125°C, as shown in Fig. 2C and fig. S26. This further suggests rearrangement of hydrogen bond networks in the MFAMs (*41*). The rearrangement proceeds without breakdown of the hydrogen bond networks, even for temperatures up to 125°C. Hence, the nanoconfined hydrogen bond networks exhibit variations in the orientational rearrangement of the hybrid

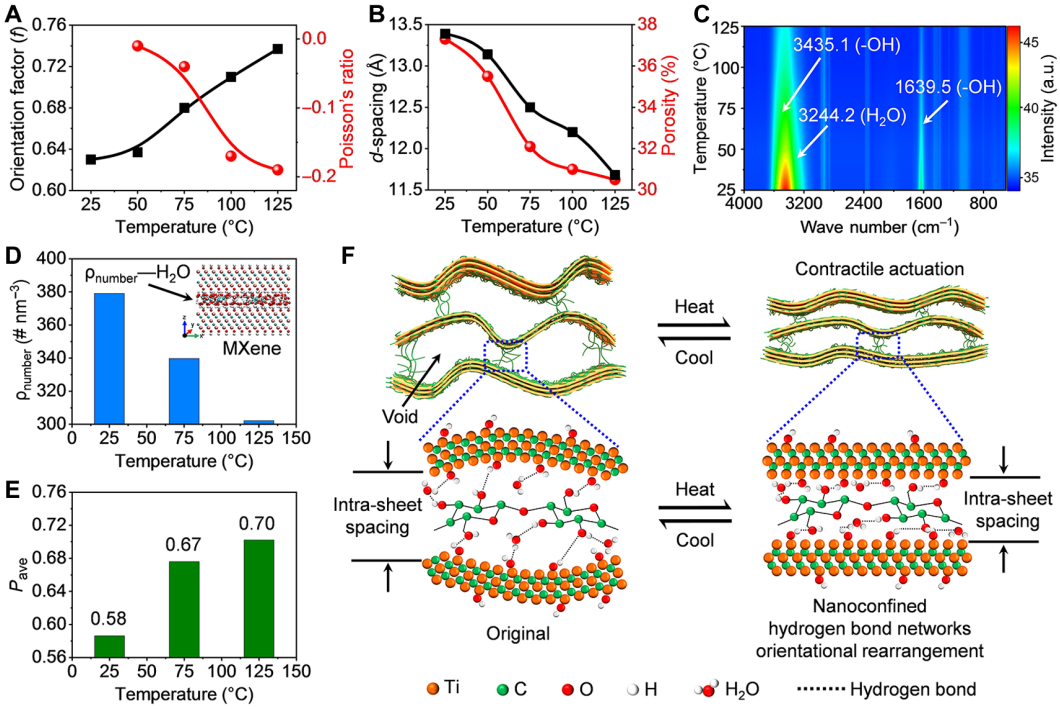

Fig. 2. In situ temperature–dependent characterization and MD simulations of the MFAMs. (**A**) The Herman's orientation factor and Poisson's ratio of the MFAMs at various temperatures. (**B**) On the basis of in situ X-ray patterns, the *d*-spacing and the calculated porosity of the MFAMs decrease with increasing temperature from 25° to 125°C. (**C**) In situ FTIR spectra of the MFAMs when heated from 25° to 125°C. (**D**) Numerical density simulation results for water molecules at the interface of the hybrid MXene/CNFs nanosheets at different temperatures. (**E**) Simulation results for the degree of parallel distribution of water molecules within hydrogen-bond networks at the interface of hybrid MXene/CNFs nanosheets when heated from 25° to 125°C. (**F**) Schematic illustration of the mechanism for the thermally driven contractile actuation of the MFAMs. The decrease in intra-sheet spacing, induced by the orientational rearrangement of nanoconfined hydrogen bond networks, leads to the flattening of hybrid MXene/CNFs nanosheets. This zipping effect reduces the void volume as the temperature increases, resulting in the large observed tensile contraction of the MFAMs.

MXene/CNFs nanosheets in the MFAMs that reduces voids, leading to large contractile actuation.

MD simulations were used to further analyze the orientational rearrangement of the nanoconfined hydrogen bond networks of the MFAMs during heating. Initially, the impact of varying numbers of water molecules within the hydrogen bond networks between hybrid MXene/CNFs nanosheets on the system's stability and its *d*-spacing were investigated in the MD simulations. As the number of water molecules increased, the *d*-spacing between hybrid MXene/CNFs nanosheets progressively expanded. Aligning with the experimental data, approximately 140 water molecules were used for this computational model (fig. S27). Consistent with experimental observations, the MD simulations demonstrate that the *d*-spacing between hybrid MXene/CNFs nanosheets gradually decreases as the temperature increases from 25° to 125°C (fig. S28), which is accompanied by the reduction in the interlayer distance by about 1.12 Å (fig. S29 and movie S2). At the same time, the number density of water molecules (ρ_{number} in # nm^{-3}) at the interface of the hybrid MXene/CNFs nanosheets decreases from ~379.1 # nm^{-3} at 25°C to ~302.2 # nm^{-3} at 125°C (Fig. 2D and fig. S30). This further shows that the reduction in intra-sheet spacing is caused by rearrangement of the hydrogen bonds during heating. As illustrated in Fig. 2E and fig. S31, the degree of parallel orientation of hydrogen bond in the network increased from ~0.58 at 25°C to ~0.70 at 125°C. In addition, although the distribution of nanoconfined hydrogen bond networks is similar throughout all intra-sheet spacings, the proportion of nanoconfined hydrogen bond networks around the 180° direction significantly increases with increasing temperature (fig. S32). These results suggest that increased orientational alignment of nanoconfined hydrogen bond networks within the orientational rearrangement of hybrid MXene/CNFs nanosheets is accompanied by reduced intra-sheet spacing, thereby inducing thermal contractile actuation of MFAMs (*42*, *43*).

The proposed mechanism for the thermally driven contractile actuation of the MFAMs is illustrated in Fig. 2F. As temperature increases, the increased alignment of the hydrogen bonds in nanoconfined networks leads to a decrease in the intra-sheet spacing. Therefore, the driving force behind contractile actuation is the flattening of the hybrid MXene/CNFs nanosheets. This creates a zipping effect that reduces the void volume as the temperature increases, resulting in large contractile actuation (*40*). The nanoconfined hydrogen bond networks return to their original orientation after cooling, allowing the MFAMs to expand.

Actuation performance of the MFAMs

The MFAMs exhibit large tensile contractile actuation in response to various stimuli, including environmental heating, electrical heating, and heating by infrared light. Moreover, the excellent mechanical properties of MXene nanosheets endow the MFAMs with high modulus in both radial and axial directions. As shown in Fig. 3 (A and B), the tensile strength of the MFAMs increases from ~53.6 MPa at 25°C to ~66.6 MPa at 125°C. These mechanical property changes

result from high temperature–induced orientational rearrangement of nanoconfined hydrogen bond networks, which results in increased overlapping of mechanical interconnected areas and densification of the MFAMs. As the temperature increases from 25° to 125°C, the Young's modulus of the MFAMs increases from ~2.8 to ~6.0 GPa. Compared to the natural and polymer fiber–based muscles (*2*–*4*, *7*, *9*, *10*, *44*–*62*), our MFAMs have much higher Young's modulus (Fig. 3C and table S5), which is extremely advantageous for actuation and commercial applications.

In addition, as shown in figs. S33 to S35, the MFAMs generated a high contractile stress of ~3.5 MPa upon heating to 125°C, when mounted on a temperature-controlled micro-tensile machine. Meanwhile, the MFAMs not only exhibited stable thermal contractile actuation but also reversibly became more electrically conducting (fig. S36) than the pristine state at 25°C due to increased overlap of mechanically interconnected areas of conducting MXene nanosheets (*16*). When the MFAMs were in the noncontracted state at 25°C, their resistance was maximum. In contrast, as the temperature increased, the resistance of the MFAMs decreased, while the contractile actuation stress increased. This opposite behavior between stress and resistance changes was attributed to the increased overlap of mechanically interconnected areas. These variations of electrical resistance during heating and cooling could potentially be used for monitoring actuation, structural integrity, and temperature. Moreover, the changes in contractile stress

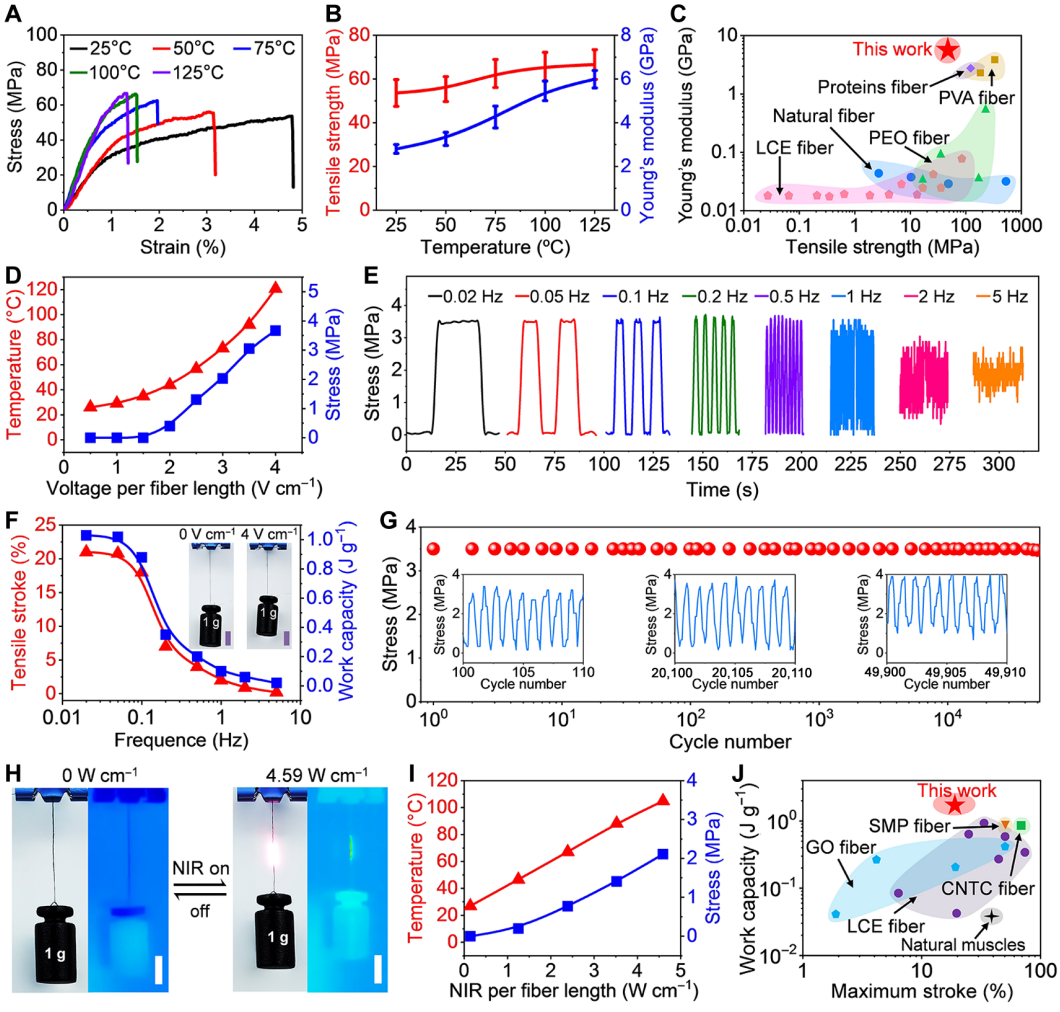

Fig. 3. Mechanical and actuation performance of the MFAMs. (**A**) Typical stress-strain curves of the MFAMs at different temperatures. (**B**) Tensile strength and Young's modulus of the MFAMs at different temperatures. (**C**) Comparison of tensile strength versus Young's modulus of the MFAMs and reported polymer fiber–based muscles including LCE fiber, poly(ethylene oxide) (PEO) fiber, proteins fiber, polyvinyl alcohol (PVA) fiber, and natural fiber. (**D**) The generated temperature and contractile actuation stress of an MFAM as a function of the applied square-wave dc voltage at 0.05 Hz. (**E**) Contractile actuation stress versus time curves for an MFAM when a square-wave dc voltage of 4 V cm^{-1} was applied at frequencies from 0.02 to 5 Hz. (**F**) The tensile strokes and work capacities of the MFAMs under a 0.64-MPa load when a 4–V cm^{-1} square-wave dc voltage at different frequencies was applied. The insets are optical photographs of tensile contraction when the applied dc voltage was increased from 0 to 4 V cm^{-1}. (**G**) Contractile actuation stress versus cycle number for an MFAM when a 1-Hz square-wave dc voltage of 4 V cm^{-1} was applied. (**H**) Optical photographs (left) and infrared thermal images (right) of an MFAM before actuation and after photothermal actuation by using an 808-nm NIR laser to deliver a power density of 4.59 W cm^{-1} to the fiber surface. (**I**) The generated temperature and contractile actuation stress of an MFAM when irradiated using different power intensities from a NIR laser. (**J**) Comparison of the work capacity versus maximum stroke of the MFAMs and reported non-twisted, thermally driven fiber-based muscles, including GO fiber, LCE fiber, SMP fiber, CNTC fiber, and natural muscles. Scale bars, 5 mm (F), 5 mm (H).

and electrical resistance of MFAMs were largely maintained during 200 cycles of heating and cooling at 0.015 Hz.

In general, MXene-based fibers, with their high electrical conductivities, are considered ideal materials for applications in thermal management and wearable heaters (*30*). As shown in figs. S37 and S38 and Fig. 3D, when 0.05-Hz square-wave dc voltages ranging from 0.5 to 4 V cm^{-1} were applied, the surface temperature of the 140-μm-diameter MFAM increased with increasing dc voltage, reversibly reaching a peak of 121.6°C when 4 V cm^{-1} was applied. A little higher voltage caused the hydrogen bond networks to begin degrading. Similar to the response observed for environmental temperature changes, the MFAMs provided fast contractile actuation upon the application of dc voltage, generating a maximum contractile actuation stress from ~0.5 to ~3.7 MPa for an applied dc voltage of 2 to 4 V cm^{-1} at a square-wave frequency of 0.05 Hz (figs. S39 and S40). Moreover, Fig. 3E illustrates that the MFAMs can generate stable, fast contractile actuation stress when subjected to a square-wave dc voltage of 4 V cm^{-1} at a frequency in the range from 0.02 to 5 Hz. However, the contractile actuation stress of the MFAMs decreased as the frequency increased from 2 to 5 Hz under the dc voltage of 4 V cm^{-1}. This decrease in actuation performance is expected because of the difficulty in thermally dissipating the generated heat to reverse actuation at high frequencies, as shown in fig. S41. The tensile strokes and work capacities of the MFAMs under a 0.64-MPa load for a 4–V cm^{-1} applied dc voltage at different frequencies are shown in Fig. 3F, fig. S42, and movie S3. As the frequency increased from 0.02 to 5 Hz, the tensile stroke and work capacity of the MFAMs decreased from 21.0% and 1.03 J g^{-1} to 0.2% and 0.02 J g^{-1}, respectively. However, contractile actuation performance maintained excellent stability more than 50,000 continuous rapid contraction cycles when a square-wave dc voltage of 4 V cm^{-1} at 1 Hz was applied (Fig. 3G and fig. S43). These obtained results indicate that the electrical stimuli have the advantages of fast response and low operating voltage, showing promising application in artificial muscles. Meanwhile, the presently used 140-μm-diameter MFAMs will deliver reduced strokes when operated at frequencies above 1 Hz. However, useful performance at higher frequencies can likely be obtained by operating these muscles in an environment that provides increased heat transfer.

The 140-μm-diameter MFAM also provided rapid photothermal actuation when exposed to infrared light. As shown in Fig. 3H and movie S4, the optical and infrared thermal images demonstrate that this diameter MFAM can lift an object weighing about 1000 times its own weight when actuated by 808-nm near-infrared (NIR) laser irradiation. The temperature increased from room temperature to 105.5°C when the muscle was exposed to this NIR laser having a power density of 4.59 W cm^{-1} (fig. S44). The contractile actuation stress of the MFAMs increased when exposed to increased power densities of the above NIR laser, and the fiber's resistance decreased (Fig. 3I and fig. S45). Our MFAMs demonstrate a maximum contractile work capacity of 1.76 J g^{-1}, which is higher than for any previously reported non-twisted, thermally driven fiber-based muscle, such as graphene oxide (GO) fiber, liquid crystal elastomer (LCE) fiber, shape memory polymer (SMP) fiber, carbon nanotube composite (CNTC) fiber, and this performance far exceeds that of natural muscles, as shown in Fig. 3J and table S6 (*3*, *4*, *8*, *46*, *48*, *49*, *60*, *63*–*69*).

Applications of the MFAMs

The abovementioned actuation performance emphasized the rapid reversible response of the MFAMs to multiple stimuli, such as environmental temperature changes and electrically produced and infrared light–generated heating. These giant stroke MFAMs present promising applications. In addition, a single MFAM fiber has high flexibility, facilitating complex deformations of the actuator. As demonstrated in Fig. 4 (A and B) and movie S5, MFAMs woven into a conventional textile can easily close and open holes in the textile when heated and cooled by 50°C. This property could be applied to temperature control clothing and smart covers designed to regulate the temperature of individuals.

We demonstrated a weight-lifting artificial arm based on four parallel 1.5-cm-long MFAMs fibers, where the needed muscle heating was provided by an NIR laser, as shown in Fig. 4C. When the artificial muscles were exposed to an 808-nm NIR laser, they rapidly contracted, causing the arm to bend to lift an ~2000 times heavier weight than the total muscle mass (Fig. 4C and movie S6). The artificial arm fully recovers to its original non-bend state when the NIR laser was turned off. During 200 investigated repeated cycles, the bending of the arm was fully reversible, as shown in Fig. 4D. This suggests that the MFAMs have excellent durability during continuous operation. In addition, Fig. 4E and movie S7 demonstrate the application of MFAMs as an infrared light–sensing robotic gripper. Eight parallel 1.5-cm-long MFAMs fibers were connected to the transmission structure of a robotic gripper. Upon NIR irradiation, the mechanical claw closed because of the contraction of the MFAMs, thereby grasping a big toy ball. The toy ball was then delivered to the destination and placed on the holder when the NIR light was turned off. We also gripped and delivered the toy ball back to its original location to verify that this task is reversible. This result shows that the MFAMs have potential applications in adaptable robotics that can perform complex tasks through photothermal actuation via remote control.

DISCUSSION

We report the large contractile actuation of MFAMs. The MXene fibers have a quite unusual structure since the MXene nanosheets are orthogonal to the fiber direction, while in ordinary MXene fibers, these nanosheets are parallel to the fiber direction. While in contrast to ordinary polymer fiber muscles or carbon nanotube fiber muscles, these new muscles are neither twisted nor coiled, the MFAMs demonstrated very useful, highly reversible contractile thermal actuation. When heated from room temperature to 125°C, these muscles contracted by 21.0%. They provided a contractile work capacity of 1.76 J g^{-1}, which is higher than for any reported prior-art non-twisted, thermally driven fiber-based muscles. This high performance of MFAMs muscles is primarily attributed to a novel actuation mechanism, which involves a change in the angle of hydrogen bonds that interconnect neighboring MXene layers, which results in the reversible elimination of void space within the MXene fibers. Despite the novel structure of these MXene fibers, they have a Young's modulus (2.8 GPa at 25°C and 6.0 GPa at 125°C) that exceeds that of conventional biological and synthetic polymers, combined with a high tensile strength of 53.6 MPa, and both of these metrics are useful for muscle applications, such as smart textiles, robotic arms, and robotic grippers.

MATERIALS AND METHODS

Materials

MAX (Ti_3AlC_2) phase powder (~400 mesh) was purchased from Jilin 11 Technology Co. LTD. CNFs were obtained from Zhongshan Nano Fiber Co. LTD. Lithium fluoride was purchased from Shanghai Maclin Biochemical Technology Co. LTD. Hydrochloric acid (HCl,

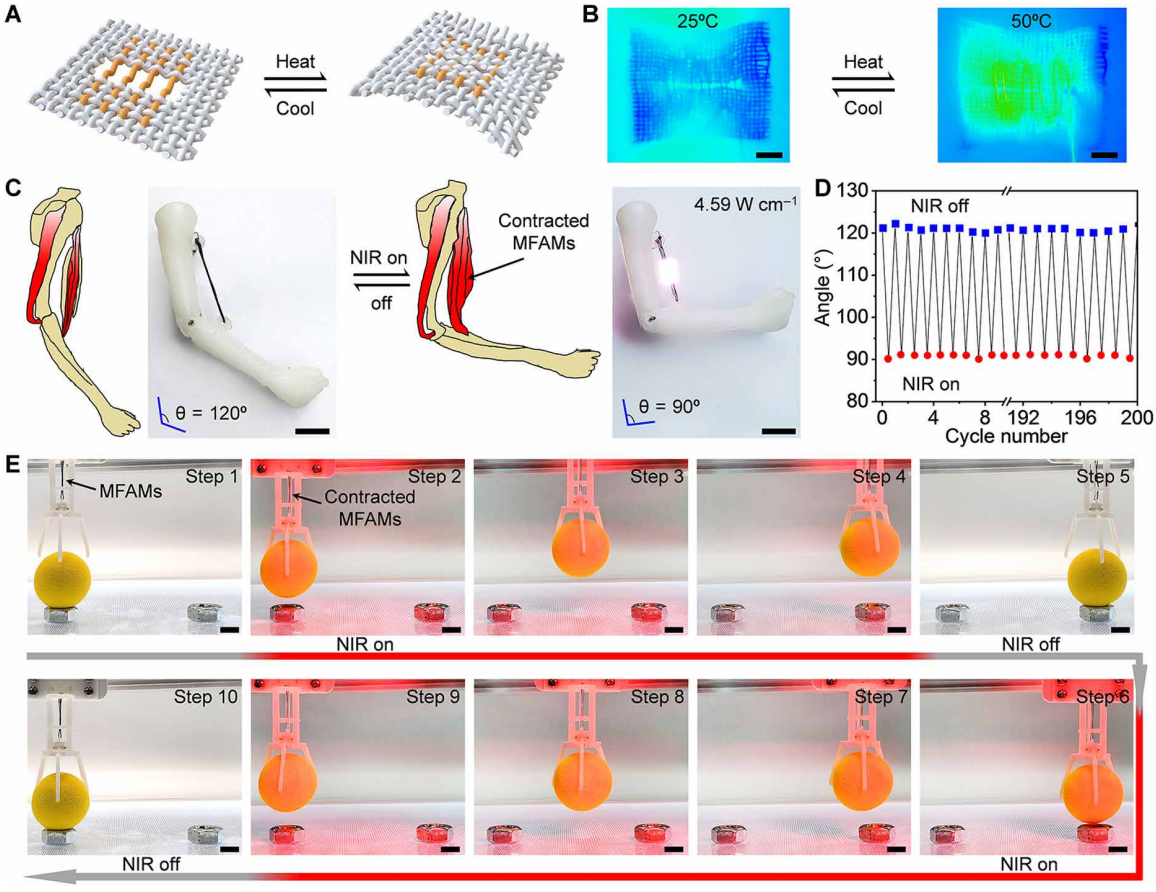

Fig. 4. Demonstration of contractile actuation of the MFAMs. (**A**) Schematic of a textile woven with MFAMs to provide heat-generated programmable shape deformation. (**B**) Infrared thermal images of thermal actuation for the textile at 25° and 50°C. (**C**) Schematic illustration and optical photographs of a weight-lifting artificial arm powered by four parallel MFAMs, which were heated by an NIR laser. When the MFAMs were exposed to an 808-nm NIR laser, they contracted like the bicep muscles of an arm. (**D**) A plot showing the angle of elbow bending during 200 repeated cycles of NIR laser–powered actuation. (**E**) Eight parallel MFAMs were combined and applied in a robotic gripper for grasping, transferring, delivering, and recovering a toy ball. Scale bars, 1 cm (B), 5 mm (C), and 5 mm (E).

GR, 36 to 38%) was supplied by Sinopharm Chemical Reagent Co. LTD. Ethanol was supplied by Modern Oriental (Beijing) Technology Development Co. LTD. All materials in this study were used in their original state and were not further purified. The deionized water used throughout the experiment was homemade by the laboratory.

Synthesis of MXene nanosheets

The MXene nanosheets were synthesized using minimally intensive delamination methods (*70*). Specifically, 3.2 g of LiF was added to 40 ml of 9 M HCl solution and dissolved. Then, 2 g of MAX powder was added to mix solution and stirred at 50°C for 30 hours. After the end of reaction and cooling to room temperature, the resultant mixture was washed seven or eight times with deionized water and centrifuged at 3500 rpm (5 min.) until the pH of supernatant was more than 6. Subsequently, the dispersion was vibrated continuously for 5 min, and this solution was centrifuged at 1500 rpm for 30 min, separating the supernatant. The remaining sediments were then subjected to several cycles of vibrations for 5 min and centrifuged at 1500 rpm for 30 min to extract more supernatant. This process was repeated until the supernatant turned light green. Next, the collected dark green supernatant was centrifuged at 4500 rpm for 20 min to obtain the sediments with the MXene nanosheets. Last, the different lateral sizes of MXene nanosheets dispersion was obtained by ultrasonicated treatment and diluting the sediments with deionized water to obtain a 3 mg ml^{-1} concentration solution. These MXene nanosheets dispersion were stored at 4°C until use.

Preparation of MFAMs via wet-spinning

The MXene/CNFs ink was obtained by mixing MXene nanosheets and CNFs dispersions to obtain weight percentage ratios of 70:30 (MFAM-I), 50:50 (MFAM-II), and 30:70 (MFAM-III) and then centrifuging this mixture to remove excess water to obtain a spinning solution having a total solid concentration of 30 mg ml^{-1}. The spinning solution was placed in a syringe and extruded through the modified nozzle into the prepared coagulant bath solution at a velocity of 300 μl min^{-1}. The modified nozzle had a diameter of 210 μm that expanded to an expansion transition diameter of 510 μm. The coagulate bath solution was ethyl alcohol. Last, the MFAMs were collected on a reel and vacuum dried for 24 hours.

Characterization

SEM images were recorded using a field-emission SEM (SU8010) at an acceleration voltage of 10 kV. TEM images were obtained using a JEM-2100F instrument with an acceleration voltage of 200 kV. HR-TEM

images were obtained by an atomic-resolved spherical aberration–corrected TEM (Themis 300) with an acceleration voltage of 300 kV. AFM images were obtained using a NanoScopeV Brooks AFM (multimode8) in tap mode. XRD patterns were obtained using a Rigaku D/max 2500 using Cu-Kα radiation and a scanning speed of 2°/min. FTIR spectroscopy spectra were collected by a Nicolet 6700 spectrometer. Thermogravimetric analysis was conducted in a nitrogen atmosphere at a heating rate of 10°C min^{-1} from room temperature to 700°C using an STA449F5. X-ray photoelectron spectroscopy spectra were collected on an ESCALABXi+ (Thermo Fisher Scientific) using a monochromatic Al-Kα X-ray source. The rheometer (Anton Paar MCR 501) was deployed to obtain the shear rheological properties and viscosity by using shear rates and vibration frequencies of 0.1 to 100 s^{-1} and 0.1 to 100 rad s^{-1}, respectively. WAXS measurements were conducted on a Xenocs Xeuss SAXS/WAXS system using an incident Cu-Kα x-ray beam (operated at 30 W). These tests used an Eiger2R 1 M detector. The sample to detector distance was 0.15 to 0.2 m, and the applied voltage and current used to generate x-rays was 50 kV and 0.6 mA.

Quantification of the WAXS patterns was conducted with scattering vector q (defined as $q = 4\pi \sin\theta/\lambda$, where 2θ is the scattering angle) and azimuthal angle φ as coordinates. The orientation of the MXene nanosheets in fibers was quantified by the (002) reflection from the WAXS patterns. The MXene nanosheets orientation and MFAMs alignment were quantified by converting the orientation distribution into an order parameter (f), defined as the following (*71*)

$$f = \frac{1}{2}\langle 3\cos^2 \emptyset - 1\rangle \quad (1)$$

where $<\cos^2\emptyset>$ is the average value of the square of the cosine of the azimuthal angle for the (002) peak of MFAMs, and the orientation factor can be expanded as (*72*)

$$\langle \cos^2 \emptyset \rangle = \frac{\int_0^{\pi/2} I(\emptyset)\cos^2\emptyset \sin\emptyset \, d\emptyset}{\int_0^{\pi/2} I(\emptyset)\sin\emptyset \, d\emptyset} \quad (2)$$

$$f = \int_0^{\pi} I(\varphi)\left(\frac{3}{2}\cos^2\emptyset - \frac{1}{2}\right)\sin(\varphi) d(\varphi) \quad (3)$$

The intensity is normalized according to

$$\int_0^{\pi} I(\varphi)\sin(\varphi) d(\varphi) = 1 \quad (4)$$

The porosities of the fabricated MFAMs were calculated according to the structural parameters via equation (*30*)

$$p(\%) = \left(1 - \frac{\rho_{MF} d_{002}}{p_M d_M}\right) \times 100 \quad (5)$$

where ρ_{MF} is the density of MFAMs, ρ_M is the MXene ($Ti_3C_2T_x$) nanosheets theoretical density of 3.68 g cm^{-3}, d_{002} is the d-spacing (002) of the MFAMs, and d_M is the d-spacing of MXene crystals (1.02 nm).

In situ XRD variable temperature tests in nitrogen atmosphere were conducted using Cu-Kα radiation, a scanning angle range of 2° to 10°, and a heating rate of 10°C min^{-1}, and the test was started after each temperature point remained constant for 2 min. In situ AFM variable temperature tests were carried out by Asylum Research instrument under Cypher ES environment using a heating rate of 10°C min^{-1}. All morphological characteristics were measured in an argon atmosphere with a tapping mode and scanning rate of 2.0 Hz. A FS-1500AuD (Olympus) needle was used. Each image has a resolution of 512 pixels by 512 pixels. In situ FTIR variable temperature tests were carried out by Frontier FTIR. In situ WAXS variable temperature tests were carried out in the Xenocs Xeuss 3.0HR equipped with the Linkam temperature stage, where the fiber sample was fixed inside the polyimide film under vacuum conditions at a heating rate of 10°C min^{-1}.

MD simulations

All MD simulations in this work were conducted using the Large-scale Atomic/Molecular Massively Parallel Simulator software package (*73*–*75*). The length, width, and height of the hybrid MXene/CNFs nanosheets interlayer interface are 32.2, 30.7, and 13.3 Å, respectively.

The equation for the orientation distribution of water molecules and hydrogen bond networks at the hybrid MXene/CNFs nanosheets interlayer interface is as follows (*6*)

$$P_{ave} = \frac{\left(3\cos^2\theta - 1\right)}{2} \quad (6)$$

where P_{ave} is the relative abundance of water molecules for hybrid MXene/CNFs nanosheets interlayer interface and θ is the orientation angle of water molecules at the hybrid MXene/CNFs nanosheets interlayer interface. An angle of 0° corresponds to water molecules oriented perpendicular to the normal z direction of the hybrid MXene/CNFs nanosheets.

Measurement of actuator performance

The contractile actuation stress of MFAMs under heat was measured by the temperature-controlled platform (TCTS 350) and the microtension machine produced by Heifei PU Liang Technology Co. Ltd. A 2.0-cm-long fiber was fixed at both ends on the fixture bracket, a 0.001-N preload force is applied to the fiber before the temperature test, and the heating and cooling rates were 50°C min^{-1}. The Joule thermal actuation performance of the fiber was studied by using Keithley 2400 dc power supply. A conductive silver adhesive was used as the contact point to connect MFAMs and conductive copper wire for loading tests. The photothermal response actuation performance of the fiber was analyzed by using a Laser WAVE infrared laser (LWIRL808-4 W-F) with laser intensity of 808 nm and laser-to-sample distance of about 30 mm. Thermal images and videos were recorded with a FOTRIC 228s infrared thermal imager when voltage and infrared laser were applied, and the emissivity was set to 0.95. The temperature-time curves were obtained by using AnalyzIR software.

Measurement for tensile stroke (ε) and work capacity (*W*)

The tensile stroke (ε) was calculated using the following Eq. 7

$$\varepsilon = \frac{L_0 - L_1}{L_0} \times 100 \quad (7)$$

where L_0 and L_1 are the initial and contracted lengths of the fiber, respectively.

The work capacity (W) was calculated using the following Eq. 8

$$W = \frac{Mgh}{m} \quad (8)$$

where M is the load suspended at the end of the fiber, g is the gravitational acceleration, h is the length of fiber contraction, and m is the weight of the fiber.

Supplementary Materials

The PDF file includes:

Supplementary Text
Figs. S1 to S45
Tables S1 to S6
Legends for movies S1 to S7

Other Supplementary Material for this manuscript includes the following:

Movies S1 to S7

REFERENCES AND NOTES

1. X. Leng, G. Mei, G. Zhang, Z. Liu, X. Zhou, Tethering of twisted-fiber artificial muscles. *Chem. Soc. Rev.* **57**, 2377–2390 (2022).
2. D. J. Roach, C. Yuan, X. Kuang, V. C.-F. Li, P. Blake, M. L. Romero, I. Hammel, K. Yu, H. J. Qi, Long liquid crystal elastomer fibers with large reversible actuation strains for smart textiles and artificial muscles. *ACS Appl. Mater. Interfaces* **11**, 19514–19521 (2019).
3. Q. He, Z. Wang, Y. Wang, Z. Wang, C. Li, R. Annapooranan, J. Zeng, R. Chen, S. Cai, Electrospun liquid crystal elastomer microfiber actuator. *Sci. Robot.* **6**, eabi9704 (2021).
4. I. H. Kim, S. Choi, J. Lee, J. Jung, J. Yeo, J. T. Kim, S. Ryu, S.-K. Ahn, J. Kang, P. Poulin, S. O. Kim, Human-muscle-inspired single fibre actuator with reversible percolation. *Nat. Nanotechnol.* **17**, 1198–1205 (2022).
5. D. Yang, M. Feng, G. Gu, High-stroke, high-output-force, fabric-lattice artificial muscles for soft robots. *Adv. Mater.* **36**, e2306928 (2023).
6. C. S. Haines, M. D. Lima, N. Li, G. M. Spinks, J. Foroughi, J. D. W. Madden, S. H. Kim, S. Fang, M. J. de Andrade, F. Göktepe, Ö. Göktepe, S. M. Mirvakili, S. Naficy, X. Lepró, J. Oh, M. E. Kozlov, S. J. Kim, X. Xu, B. J. Swedlove, G. G. Wallace, R. H. Baughman, Artificial muscles from fishing line and sewing thread. *Science* **343**, 868–872 (2014).
7. M. Kanik, S. Orguc, G. Varnavides, J. Kim, T. Benavides, D. Gonzalez, T. Akintilo, C. C. Tasan, A. P. Chandrakasan, Y. Fink, P. Anikeeva, Strain-programmable fiber-based artificial muscle. *Science* **365**, 145–150 (2019).
8. Y. Cui, J. Lin, Y. Zhai, C. Xu, C. Chen, C. Chang, Hydration programmable, shape memorable artificial muscles for antagonistic movements. *Adv. Funct. Mater.* **34**, 2401005 (2024).
9. B. Cui, M. Ren, L. Dong, Y. Wang, J. He, X. Wei, Y. Zhao, P. Xu, X. Wang, J. Di, Q. Li, Pretension-free and self-recoverable coiled artificial muscle fibers with powerful cyclic work capability. *ACS Nano* **17**, 12809–12819 (2023).
10. C. Lang, E. C. Lloyd, K. E. Matuszewski, Y. Xu, V. Ganesan, R. Huang, M. Kumar, R. J. Hickey, Nanostructured block copolymer muscles. *Nat. Nanotechnol.* **17**, 752–758 (2022).
11. H. Chu, X. Hu, Z. Wang, J. Mu, N. Li, X. Zhou, S. Fang, C. S. Haines, J. W. Park, S. Qin, N. Yuan, J. Xu, S. Tawfick, H. Kim, P. Conlin, M. Cho, K. Cho, J. Oh, S. Nielsen, K. A. Alberto, J. M. Razal, J. Foroughi, G. M. Spinks, S. J. Kim, J. Ding, J. Leng, R. H. Baughman, Unipolar stroke, electroosmotic pump carbon nanotube yarn muscles. *Science* **371**, 494–498 (2021).
12. L. Dong, M. Ren, Y. Wang, G. Wang, S. Zhang, X. Wei, J. He, B. Cui, Y. Zhao, P. Xu, X. Wang, J. Di, Q. Li, Artificial neuromuscular fibers by multilayered coaxial integration with dynamic adaption. *Sci. Adv.* **8**, eabq7703 (2022).
13. M. D. Lima, N. Li, M. J. de Andrade, S. Fang, J. Oh, G. M. Spinks, M. E. Kozlov, C. S. Haines, D. Suh, J. Foroughi, S. J. Kim, Y. Chen, T. Ware, M. K. Shin, L. D. Machado, A. F. Fonseca, J. D. W. Madden, W. E. Voit, D. S. Galvão, R. H. Baughman, Electrically, chemically, and photonically powered torsional and tensile actuation of hybrid carbon nanotube yarn muscles. *Science* **338**, 928–932 (2012).
14. J. Mu, M. J. de Andrade, S. Fang, X. Wang, E. Gao, N. Li, S. H. Kim, H. Wang, C. Hou, Q. Zhang, M. Zhu, D. Qian, H. Lu, D. Kongahage, S. Talebian, J. Foroughi, G. Spinks, H. Kim, T. H. Ware, H. J. Sim, D. Y. Lee, Y. Jang, S. J. Kim, R. H. Baughman, Sheath-run artificial muscles. *Science* **365**, 150–155 (2019).
15. P. Chen, Y. Xu, S. He, X. Sun, S. Pan, J. Deng, D. Chen, H. Peng, Hierarchically arranged helical fibre actuators driven by solvents and vapours. *Nat. Nanotechnol.* **10**, 1077–1083 (2015).
16. A. VahidMohammadi, J. Rosen, Y. Gogotsi, The world of two-dimensional carbides and nitrides (MXenes). *Science* **372**, eabf1581 (2021).
17. M. Naguib, M. Kurtoglu, V. Presser, J. Lu, J. Niu, M. Heon, L. Hultman, Y. Gogotsi, M. W. Barsoum, Two-Dimensional nanocrystals produced by exfoliation of Ti_3AlC_2. *Adv. Mater.* **23**, 4248–4253 (2011).
18. M. Han, C. E. Shuck, R. Rakhmanov, D. Parchment, B. Anasori, C. M. Koo, G. Friedman, Y. Gogotsi, Beyond $Ti_3C_2T_x$: MXenes for electromagnetic interference shielding. *ACS Nano* **14**, 5008–5016 (2020).
19. M. Ghidiu, M. R. Lukatskaya, M. Q. Zhao, Y. Gogotsi, M. W. Barsoum, Conductive two-dimensional titanium carbide 'clay' with high volumetric capacitance. *Nature* **516**, 78–81 (2014).
20. J. Zhang, N. Kong, S. Uzun, A. Levitt, S. Seyedin, P. A. Lynch, S. Qin, M. Han, W. Yang, J. Liu, X. Wang, Y. Gogotsi, J. M. Razal, Scalable manufacturing of free-standing, strong $Ti_3C_2T_x$ MXene films with outstanding conductivity. *Adv. Mater.* **32**, e2001093 (2020).
21. A. Iqbal, F. Shahzad, K. Hantanasirisakul, M.-K. Kim, J. Kwon, J. Hong, H. Kim, D. Kim, C. M. Koo, Y. Gogotsi, C. M. Koo, Anomalous absorption of electromagnetic waves by 2D transition metal carbonitride Ti_3CNT_x (MXene). *Science* **369**, 446–450 (2020).
22. F. Shahzad, M. Alhabeb, C. B. Hatter, B. Anasori, S. M. Hong, C. M. Koo, Y. Gogotsi, Electromagnetic interference shielding with 2D transition metal carbides (MXenes). *Science* **353**, 1137–1140 (2016).
23. B. Anasori, M. R. Lukatskaya, Y. Gogotsi, 2D metal carbides and nitrides (MXenes) for energy storage. *Nat. Rev. Mater.* **2**, 16098 (2017).
24. B. Thomas, M. C. Raj, A. K. B., R. M. H., J. Joy, A. Moores, G. L. Drisko, C. Sanchez, Nanocellulose, a versatile green platform: From biosources to materials and their applications. *Chem. Rev.* **118**, 11575–11625 (2018).
25. E. Kontturi, P. Laaksonen, M. B. Linder, N. , A. H. Gröschel, O. J. Rojas, O. Ikkala, Advanced materials through assembly of nanocelluloses. *Adv. Mater.* **30**, 1703779 (2018).
26. G. Cai, J.-H. Ciou, Y. Liu, Y. Jiang, P. S. Lee, Leaf-inspired multiresponsive MXene-based actuator for programmable smart devices. *Sci. Adv.* **5**, eaaw7956 (2019).
27. G. Xin, W. Zhu, Y. Deng, J. Cheng, L. T. Zhang, A. J. Chung, S. De, J. Lian, Microfluidics-enabled orientation and microstructure control of macroscopic graphene fibres. *Nat. Nanotechnol.* **14**, 168–175 (2019).
28. S. Wan, X. Li, Y. Wang, Y. Chen, X. Xie, R. Yang, A. P. Tomsia, L. Jiang, Q. Cheng, Strong sequentially bridged MXene sheets. *Proc. Natl. Acad. Sci. U.S.A.* **117**, 27154–27161 (2020).
29. A. Lipatov, H. Lu, M. Alhabeb, B. Anasori, A. Gruverman, Y. Gogotsi, A. Sinitskii, Elastic properties of 2D $Ti_3C_2T_x$ MXene monolayers and bilayers. *Sci. Adv.* **4**, eaat0491 (2018).
30. T. Zhou, Y. Yu, B. He, Z. Wang, T. Xiong, Z. Wang, Y. Liu, J. Xin, M. Qi, H. Zhang, X. Zhou, L. Gao, Q. Cheng, L. Wei, Ultra-compact MXene fibers by continuous and controllable synergy of interfacial interactions and thermal drawing-induced stresses. *Nat. Commun.* **13**, 4564 (2022).
31. Z. Zeng, C. Wang, G. Siqueira, D. Han, A. Huch, S. Abdolhosseinzadeh, J. Heier, F. Nüesch, C. Zhang, G. Nyström, Nanocellulose-MXene biomimetic aerogels with orientation-tunable electromagnetic interference shielding performance. *Adv. Sci.* **7**, 2000979 (2020).
32. W.-T. Cao, F.-F. Chen, Y.-J. Zhu, Y.-G. Zhang, Y.-Y. Jiang, M.-G. Ma, F. Chen, Binary strengthening and toughening of MXene/cellulose nanofiber composite paper with nacre-inspired structure and superior electromagnetic interference shielding properties. *ACS Nano* **12**, 4583–4593 (2018).
33. J. Yang, R. Dettori, J. P. F. Nunes, N. H. List, E. B. Centurion, Z. Chen, A. A. Cordones, D. P. Deponte, T. F. Heinz, M. E. Kozina, K. Ledbetter, M.-F. Lin, A. M. Lindenberg, M. Mo, A. Nilsson, X. Shen, T. J. A. Wolf, D. Donadio, K. J. Gaffney, T. J. Martinez, X. Wang, Direct observation of ultrafast hydrogen bond strengthening in liquid water. *Nature* **596**, 531–535 (2021).
34. W. Eom, H. Shin, R. B. Ambade, S. H. Lee, K. H. Lee, D. J. Kang, T. H. Han, Large-scale wet-spinning of highly electroconductive MXene fibers. *Nat. Commun.* **11**, 2825 (2020).
35. Y. Xia, T. S. Mathis, M.-Q. Zhao, B. Anasori, A. Dang, Z. Zhou, H. Cho, Y. Gogotsi, S. Yang, Thickness-independent capacitance of vertically aligned liquid-crystalline MXenes. *Nature* **557**, 409–412 (2018).
36. M. Trebbin, D. Steinhauser, J. Perlich, A. Buffet, S. V. Roth, W. Zimmermann, J. Thiele, S. Förster, Anisotropic particles align perpendicular to the flow direction in narrow microchannels. *Proc. Natl. Acad. Sci. U.S.A.* **110**, 6706–6711 (2013).
37. M. Shekhirev, C. E. Shuck, A. Sarycheva, Y. Gogotsi, Characterization of MXenes at every step, from their precursors to single flakes and assembled films. *Prog. Mater. Sci.* **120**, 100757 (2021).
38. H. Zhu, S. Zhu, Z. Jia, S. Parvinian, Y. Li, O. Vaaland, L. Hu, T. Li, Anomalous scaling law of strength and toughness of cellulose nanopaper. *Proc. Natl. Acad. Sci. U.S.A.* **112**, 8971–8976 (2015).
39. T. Li, C. Chen, A. H. Brozena, J. Y. Zhu, L. Xu, C. Driemeier, J. Dai, O. J. Rojas, A. Isogai, L. Wågberg, L. Hu, Developing fibrillated cellulose as a sustainable technological material. *Nature* **590**, 47–56 (2021).
40. H. Wang, X. Sun, Y. Wang, K. Li, J. Wang, X. Dai, B. Chen, D. Chong, L. Zhang, J. Yan, Acid enhanced zipping effect to densify MWCNT packing for multifunctional MWCNT films with ultra-high electrical conductivity. *Nat. Commun.* **14**, 380 (2023).

41. L. Zhang, S. Wang, Z. Wang, Z. Liu, X. Xu, H. Liu, D. Wang, Z. Tian, Temperature-mediated phase separation enables strong yet reversible mechanical and adhesive hydrogels. *ACS Nano* **17**, 13948–13960 (2023).
42. M. Lounasvuori, Y. Sun, T. S. Mathis, L. Puskar, U. Schade, D.-E. Jiang, Y. Gogotsi, T. Petit, Vibrational signature of hydrated protons confined in MXene interlayers. *Nat. Commun.* **14**, 1322 (2023).
43. J. Yang, M. Li, S. Fang, Y. Wang, H. He, C. Wang, Z. Zhang, B. Yuan, L. Jiang, R. H. Baughman, Q. Cheng, Water-induced strong isotropic MXene-bridged graphene sheets for electrochemical energy storage. *Science* **383**, 771–777 (2024).
44. M. C. Escobar, T. J. White, Fast and slow-twitch actuation via twisted liquid crystal elastomer fibers. *Adv. Mater.* **36**, 2401140 (2024).
45. J. Naciri, A. Srinivasan, H. Jeon, N. Nikolov, P. Keller, B. R. Ratna, Nematic elastomer fiber actuator. *Macromolecules* **36**, 8499–8505 (2003).
46. D. Wu, Y. Zhang, H. Yang, A. Wei, Y. Zhang, A. Mensah, R. Yin, P. Lv, Q. Feng, Q. Wei, Scalable functionalized liquid crystal elastomer fiber soft actuators with multi-stimulus responses and photoelectric conversion. *Mater. Horiz.* **10**, 2587–2598 (2023).
47. Z. Hu, Y. Li, T. Zhao, J. Lv, Self–winding liquid crystal elastomer fiber actuators with high degree of freedom and tunable actuation. *Appl. Mater. Today* **27**, 101449 (2022).
48. A. Kotikian, J. M. Morales, A. Lu, J. Mueller, Z. S. Davidson, J. W. Boley, J. A. Lewis, Innervated, self–sensing liquid crystal elastomer actuators with closed loop control. *Adv. Mater.* **33**, e2101814 (2021).
49. J. Liu, Y. Gao, H. Wang, R. Poling-Skutvik, C. O. Osuji, S. Yang, Shaping and locomotion of soft robots using filament actuators made from liquid crystal elastomer–carbon nanotube composites. *Adv. Intell. Syst.* **2**, 1900163 (2020).
50. A. P. Martinez, A. Ng, S. H. Nah, S. Yang, Active-textile yarns and embroidery enabled by wet-spun liquid crystalline elastomer filaments. *Adv. Funct. Mater.* **34**, 2400742 (2024).
51. C. Zhang, G. Fei, X. Lu, H. Xia, Y. Zhao, Liquid crystal elastomer artificial tendrils with asymmetric core–sheath structure showing evolutionary biomimetic locomotion. *Adv. Mater.* **36**, e2307210 (2024).
52. Y. Yu, L. Li, E. Liu, X. Han, J. Wang, Y. X. Xie, C. Lu, Light-driven core–shell fiber actuator based on carbon nanotubes/liquid crystal elastomer for artificial muscle and phototropic locomotion. *Carbon* **187**, 97–107 (2022).
53. J. Sun, H. He, K. Zhao, W. Cheng, Y. Li, P. Zhang, S. Wan, Y. Liu, M. Wang, M. Li, Z. Wei, B. Li, Y. Zhang, C. Li, Y. Sun, J. Shen, J. Li, F. Wang, C. Ma, Y. Tian, J. Su, D. Chen, C. Fan, H. Zhang, K. Liu, Protein fibers with self-recoverable mechanical properties via dynamic imine chemistry. *Nat. Commun.* **14**, 5348 (2023).
54. Y. Wu, D. U. Shah, B. Wang, J. Liu, X. Ren, M. H. Ramage, O. A. Scherman, Biomimetic supramolecular fibers exhibit water-induced supercontraction. *Adv. Mater.* **30**, e1707169 (2018).
55. J. Yuan, W. Neri, C. Zakri, P. Merzeau, K. Kratz, A. Lendlein, P. Poulin, Shape memory nanocomposite fibers for untethered high-energy microengines. *Science* **365**, 155–158 (2019).
56. J. Yi, G. Zou, J. Huang, X. Ren, Q. Tian, Q. Yu, P. Wang, Y. Yuan, W. Tang, C. Wang, L. Liang, Z. Cao, Y. Li, M. Yu, Y. Jiang, F. Zhang, X. Yang, W. Li, X. Wang, Y. Luo, X. J. Loh, G. Li, B. Hu, Z. Liu, H. Gao, X. Chen, Water-responsive supercontractile polymer films for bioelectronic interfaces. *Nature* **624**, 295–302 (2023).
57. M. H. Li, P. Keller, J. Yang, P. A. Albouy, An artificial muscle with lamellar structure based on a nematic triblock copolymer. *Adv. Mater.* **16**, 1922–1925 (2004).
58. M. Duduta, R. J. Wood, D. R. Clarke, Multilayer dielectric elastomers for fast, programmable actuation without prestretch. *Adv. Mater.* **28**, 8058–8063 (2016).
59. S. M. Mirvakili, I. W. Hunter, Artificial muscles: Mechanisms, applications, and challenges. *Adv. Mater.* **30**, 10.1002/adma.201704407 (2018).
60. C. D. Kuthe, R. V. Uddanwadiker, Investigation of effect of fiber orientation on mechanical behavior of skeletal muscle. *J. Appl. Biomater. Funct. Mater.* **14**, e154–e162 (2016).
61. D. Liu, A. Tarakanova, C. C. Hsu, M. Yu, S. Zheng, L. Yu, J. Liu, Y. He, D. J. Dunstan, M. J. Buehler, Spider dragline silk as torsional actuator driven by humidity. *Sci. Adv.* **5**, eaau9183 (2019).
62. R. L. McGough, R. E. Debski, E. Taskiran, F. H. Fu, S. L. Y. Woo, Mechanical properties of the long head of the biceps tendon. *Knee Surg. Sports Traumatol. Arthrosc.* **3**, 226–229 (1996).
63. W. Hou, J. Wang, J. Lv, Bioinspired liquid crystalline spinning enables scalable fabrication of high-performing fibrous artificial muscles. *Adv. Mater.* **35**, e2211800 (2023).
64. H. Kim, Y. Jang, D. Y. Lee, J. H. Moon, J. G. Choi, G. M. Spinks, S. Gambhir, D. L. Officer, G. G. Wallace, S. J. Kim, Bio-inspired stretchable and contractible tough fiber by the hybridization of GO/MWNT/polyurethane. *ACS Appl. Mater. Interfaces* **11**, 31162–31168 (2019).
65. J. Oh, M. E. Kozlov, J. Carretero-González, E. Castillo-Martínez, R. H. Baughman, Thermal actuation of graphene oxide nanoribbon mats. *Chem. Phys. Lett.* **505**, 31–36 (2011).
66. W. Wang, C. Xiang, D. Sun, M. Li, K. Yan, D. Wang, Photothermal and moisture actuator made with graphene oxide and sodium alginate for remotely controllable and programmable intelligent devices. *ACS Appl. Mater. Interfaces* **11**, 21926–21934 (2019).
67. K. Chen, M. Li, Z. Yang, Z. Ye, D. Zhang, B. Zhao, Z. Xia, Q. Wang, X. Kong, Y. Shang, C. Liu, H. Yu, A. Cao, Ultra-large stress and strain polymer nanocomposite actuators incorporating a mutually-interpenetrated, collective-deformation carbon nanotube network. *Adv. Mater.* **36**, e2313354 (2024).
68. S. Sarikaya, F. Gardea, H. Strong, J. T. Auletta, D. M. Mackie, M. Naraghi, Tunable actuation of humidity-driven artificial muscles via graphene nanofillers. *ACS Appl. Polym. Mater.* **4**, 8803–8811 (2022).
69. D. Wu, X. Li, Y. Zhang, X. Cheng, Z. Long, L. Ren, X. Xia, Q. Wang, J. Li, P. Lv, Q. Feng, Q. Wei, Novel biomimetic "spider web" robust, super-contractile liquid crystal elastomer active yarn soft actuator. *Adv. Sci.* **11**, e2400557 (2024).
70. M. Alhabeb, K. Maleski, B. Anasori, P. Lelyukh, L. Clark, S. Sin, Y. Gogotsi, Guidelines for synthesis and processing of two-dimensional titanium carbide ($Ti_3C_2T_x$ MXene). *Chem. Mater.* **29**, 7633–7644 (2017).
71. H. Park, K. H. Lee, Y. B. Kim, S. B. Ambade, S. H. Noh, W. Eom, J. Y. Hwang, W. J. Lee, J. Huang, T. H. Han, Dynamic assembly of liquid crystalline graphene oxide gel fibers for ion transport. *Sci. Adv.* **4**, eaau2104 (2018).
72. S. Wan, X. Li, Y. Chen, N. Liu, S. Wang, Y. Du, Z. Xu, X. Deng, S. Dou, L. Jiang, Q. Cheng, Ultrastrong MXene films via the synergy of intercalating small flakes and interfacial bridging. *Nat. Commun.* **13**, 7340 (2022).
73. S. Plimpton, Fast parallel algorithms for short-range molecular dynamics. *J. Comput. Phys.* **117**, 1–19 (1995).
74. R. W. Hockney, J. Eastwood, *Computer simulation using particles* (Taylor & Francis Inc. 1988).
75. H. J. C. Berendsen, J. P. M. Postma, W. F. van Gunsteren, A. DiNola, J. R. Haak, Molecular dynamics with coupling to an external bath. *J. Comput. Phys.* **81**, 3684–3690 (1984).

Acknowledgments: We thank Y. Sun at Institute of Chemistry, Chinese Academy of Sciences for in situ XRD testing; Y. Liu at Beihang University for in situ WAXS testing; S. Yue at Tsinghua University for in situ AFM testing; W. Wang at Beihang University for in situ FTIR testing; G. Li at Beihang University for taking and processing FIB-SEM images; X. Yang and X. Li at Technical Institute of Physics and Chemistry, Chinese Academy of Sciences for TEM testing; and K. Qiu at Beihang University for HR-TEM testing. We thank the High-Performance Computing Platform at Beihang University, the assistance with nano-CT characterization at the Analysis and Testing Center of Beihang University, and the Physical and Chemical Analysis Center at Suzhou Institute for Advanced Research, University of Science and Technology of China. **Funding:** This work was supported by the National Science Fund for Distinguished Young Scholars (grant no. 52125302) to Q.C., the National Key Research and Development Program of China (grant no. 2021YFA0715700) to Q.C., the National Natural Science Foundation of China (grants no. 52350012 and 22075009) to Q.C., the New Cornerstone Science Foundation through the XPLORER PRIZE to Q.C., and the Robert A. Welch Foundation (grant no. AT-0029) to US participant R.H.B.. **Author contributions:** Conceptualization: Q.C. Methodology: J.F., Y.L., T.Z., Y.W., M.Z., K.L., and W.L. Investigation: Q.C., J.F., and Y.L. Visualization: Q.C. Supervision: Q.C. Writing—original draft: J.F., Y.L., T.Z., S.F., M.Z., R.H.B., L.W., and Q.C. Writing—review and editing: J.F., Y.L., S.F., M.Z., R.H.B., and Q.C. **Competing interests:** Q.C., J.F., Y.L., and T.Z. are inventors on Chinese patent application 202411560950.X submitted by Beihang University, which covers the method for fabricating radially oriented MXene composite fiber tensile artificial muscles. The authors declare that they have no other competing interests. **Data and materials availability:** All data needed to evaluate the conclusions in the paper are present in the paper and/or the Supplementary Materials.

Submitted 14 September 2024
Accepted 4 December 2024
Published 8 January 2025
10.1126/sciadv.adt1560